von KARMAN INSTITUTE
FOR FLUID DYNAMICS

TULabs

Diederik Beckers, Riccardo Rubini, Nikolaos Vasilakopoulos

November 2016

Contents

Nomenclature

α absolute flow angle

β relative flow angle

γ heat capacity ratio

BPF   blade passing frequency

RF   rotational frequency

RSF   rotating stall frequency

SF   stall frequency

Ω rotation speed

ω loss coefficient or angular frequency

ϕ flow coefficient

ψ load coefficient

ρ density

σ standard deviation

τ time constant

c speed of sound

f frequency

H percentage span

h enthalpy

P pressure

R universal gas constant

r radius

T temperature

U blade velocity

V absolute velocity

v	voltage
W	relative velocity

Subscripts

0	fundamental frequency
1	upstream section or first
2	downstream section or second
amb	ambient
dyn	dynamic
s	static
tot	total
θ	tangential
z	axial

Superscripts

R	relative

1 Introduction

The purpose of this short campaign was to familiarise with turbomachinery facilities and some measurement techniques in terms of calibration, data acquisition-processing and commenting on results. The main objectives were to perform performance measurements in a compressor test rig and investigate its behaviour close to stall.

As soon as the probes were calibrated, several pressure measurements were taken at different span heights (for 1000 rpm and 100% throttle opening) in order to characterise the flow upstream and downstream of the rotor. Before each measurement the probe was aligned to the flow by turning it using a protractor in order to have $P_{\text{left}} - P_{\text{right}} = 0$. In total, three differential pressure measurements were taken each time:

- P_{tot}-P_{amb},

- P_{tot}-P_{s},

- P_{left}-P_{right}.

For the performance map and the investigation of stall onset, a hot-wire probe was placed upstream of the rotor in order to take velocity-fluctuations measurements. These measurements were performed at a certain span-height (50%) for different throttle positions until stall.

2 Test setup

2.1 Facility description

The R1 facility consists of a low speed-axial 1.5-stage compressor connected to an open loop wind tunnel. The rotor of the stage has 25 blades while the stator has 25 outlet guide vanes. There are also 39 inlet guide vanes before the rotor to deliver a desirable swirl to the rotor. The compressor shaft is driven by a 75 hp DC motor which rotates it clockwise up to 1500 rpm. The mass flow is adjusted by a throttle valve (at the end of the tunnel) whose opening is adjusted by a throttle control device from 15% to 100%. A speed control adjuster is used to define the desirable rpm to the compressor while the actual value of the rotation speed is displayed from a tachometer (in Hz).
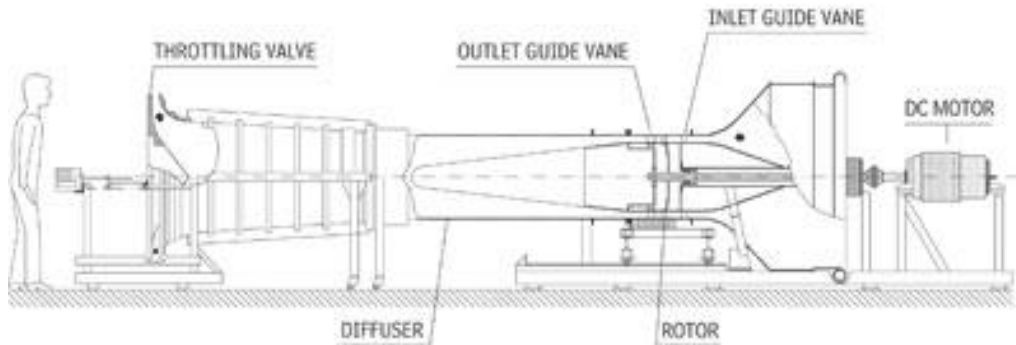

Figure 1: Facility General Arrangement

The probes used for the pressure measurements are 2 NACA short prism probes, which are shown in Fig. 2. These probes are placed upstream and downstream of the rotor, shown in Fig. 3 and schematically in Fig. 6. These probes can measure total and static pressure as well as the flow yaw angle. They are incorporated in an adjusting screw which enables us to adjust the measurement span height and to align the probe with the flow. The value of the flow angle is taken from a goniometer at the bottom of the screw.
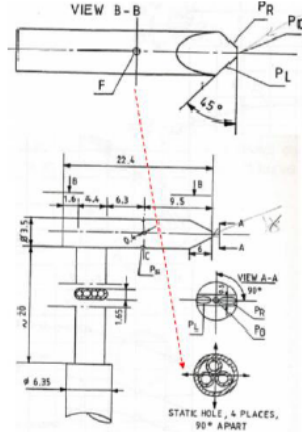

Figure 2: Pressure measurement NACA probes

Figure 3: Probes arrangement

The probes are connected to three Validyne transducers through pneumatic lines. Three-way valves, such as shown in Fig. 4, are used to switch between upstream and downstream probes. The pneumatic lines are connected to the transducers such as in Fig. 6 in order to obtain the differential pressure mentioned above. The ambient pressure is probed in a bottle exposed to the environment in order to avoid local fluctuations.

Each transducer is connected to an amplifier shown in Fig. 5. The final data are acquired by the acquisition system (6-channel Nicolet BE256-M1 connected with a PC). A multimeter is also available for quicker calibration and adjustment of the transducers. So, four channels of the acquisition system are finally occupied, three for the pressure transducers and one for the hot-wire probe.

Figure 4: Switching valve

Figure 5: Amplifiers and Multimeters

In order to measure the high-frequency velocity fluctuations, a single hot-wire probe is placed upstream of the rotor, shown in Fig. 7 and schematically in Fig. 6. The installation arrangement is

similar with that of the pressure probes, so it is feasible to rotate it in order to set it in a normal position to the flow. The hot-wire probe is connected to a dedicated electronic circuit (shown in Fig. 8) which enables us to adjust the wire's resistance, response and sensitivity. Moreover, an oscilloscope is used in order to optimise the response time of the wire.
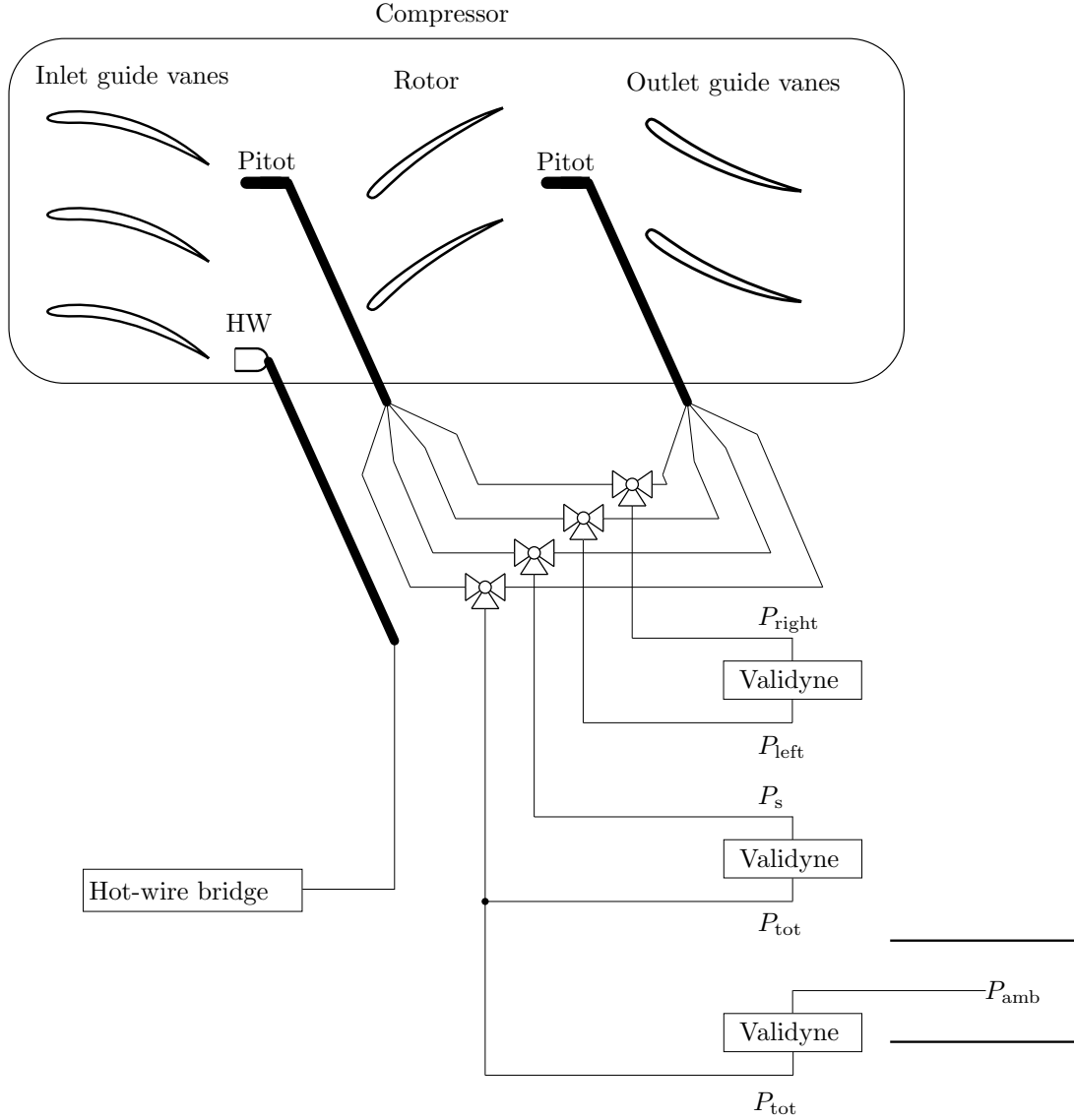
Figure 6: Measurement setup.

Figure 7: Hot-wire arrangement


Figure 8: Hot-wire's electronics

2.2 Pressure transducers calibration

Three Validyne differential pressure transducers were used for the pressure measurements mentioned above. This type of transducers contains thin membranes whose deformation corresponds to the pressure difference between inlet and outlet port. The maximum pressure difference that the particular membranes can withstand before plastic deformation occurs is about 86 mbar.

At the beginning, the transducers had to be tested for leakage. A Druck pressure calibrator was used in order to apply accurate pressure values. Both ports of the three transducers were connected to the calibrator and the pressure was set to 80 mbar(max). So, each transducer had to be tested separately so that the calibrator's pressure indication was constant. Fluctuations of 0.1 mbar/10 sec magnitude were ignored.

The amplifiers had to be calibrated (this time all together connected with tees). One port of each transducer were connected to the calibrator and the other was free to P_{amb}. The pressure's calibrator indication was reset to zero and the amplifiers voltage (measured by a multimeter) was also adjusted approximately to zero by turning the "Zero" knot. Then maximum pressure (80 mbar) was applied by the pressure calibrator and the voltage output was adjusted to +5 V by turning the "Span" knob. The same procedure was repeated for −80 mbar and −5 V respectively.

Finally, different pressure from -80 to 80 mbar with a step of 10 mbar was applied to the transducers in order to extract their calibration curves. The voltages for each pressure were recorded by the acquisition system, the time-resolved measurements were averaged for each pressure value and the curves were extracted. All the transducers presented satisfactory linearity ($R^2 = 0,9998 − 1$). The calibration curves and their functions are presented in figure 9.
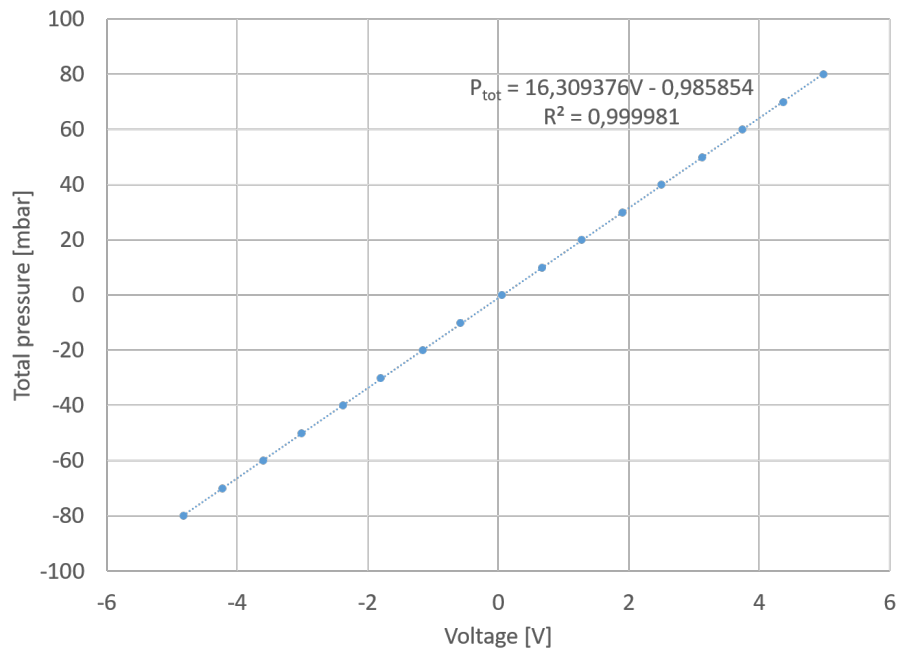
(a) Total pressure
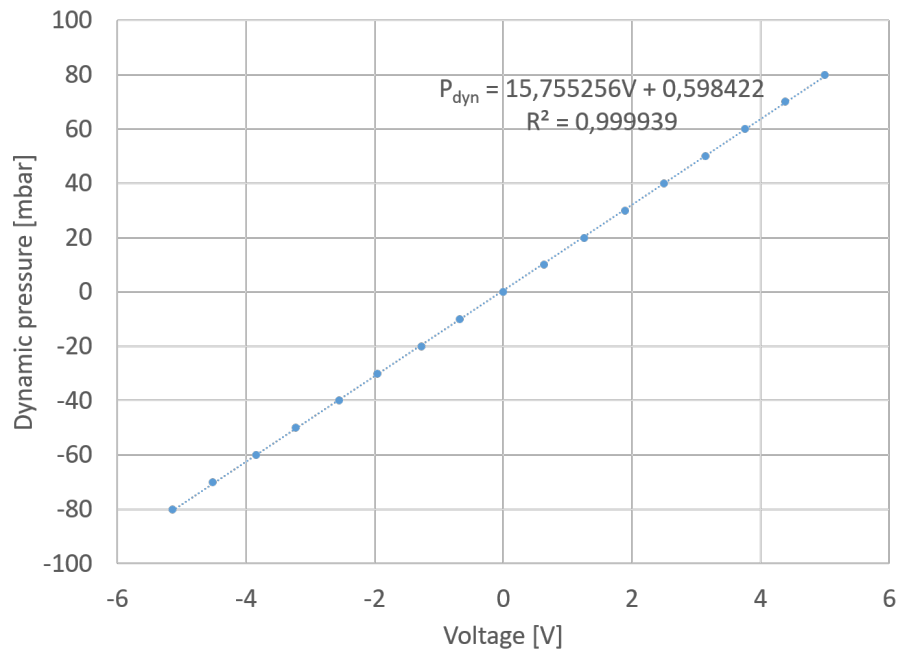
(b) Dynamic pressure

Figure 9: Calibration curves

3 Flow measurement

This part of the report presents the measured and calculated flow quantities in two sections. The first section is between the inlet guide vanes and the rotor and is denoted as the upstream section. The second section is between the rotor and the outlet guide vanes and is denoted as the downstream section. The flow quantities in the upstream and downstream section are indicated by the subscript 1 and 2 respectively.

The measurements and calculations allow to reconstruct the profiles of the velocities, pressure, flow angles, work distribution, specific angular momentum, turning and losses over the range from 10 % span to 90 % span. These measurements were taken at a throttle position of 100 % and a rotation speed of 1000 rpm.

3.1 Measurement procedure

The test setup provides measurements of the total pressure, dynamic pressure and the absolute flow angle. These measurements are taken in both the upstream and downstream section from 10 % span up to 90 % span with 10 % increments. The different span positions and their radial coordinates are listed in Table 1. This results in a total of eighteen measurements. Note that in this part of the measurement campaign, only the data of the pressure probes is used and the hot-wire data is neglected The measured quantities were recorded at a sampling frequency of 183 Hz over a time of 2 s.

Span [%]	Radial coordinate [m]
10	0.2845
20	0.292
30	0.2995
40	0.307
50	0.3145
60	0.322
70	0.3295
80	0.337
90	0.3445

Table 1: Spanwise positions at which the measurements were taken.

3.2 Postprocessing

The measurements allow to calculate the relevant flow quantities in the upstream and downstream section at each spanwise position.

Pressures

The ambient conditions at the time of the measurements were different from the ambient conditions during the calibration of the pressure transducers. This resulted in the zero errors listed in Table 2 which had to be taken into account during the postprocessing.

The total pressure P_{tot} and dynamic pressure P_{dyn} were obtained by averaging the recorded data and applying the conversion formula of the calibration curve taking the zero error into account and adding the ambient pressure in the case of the total pressure. The static pressure was calculated as the difference between the total and dynamic pressure:

$$P_{\text{s}} = P_{\text{tot}} - P_{\text{dyn}} \,. \tag{1}$$

Transducer	Zero error [V]
P_{tot}	-0.32
P_{dyn}	-0.33
P_{lr}	-0.34

Table 2: Zero errors at the time of measurement.

Velocities and flow angles

The absolute velocity V, relative velocity W, absolute flow angle α and relative flow angle β are defined such as in Fig. 10 with the flow angles positive as shown in the figure. The tangential component of a velocity is considered positive in the direction of rotation. The blade velocity U is calculated at each spanwise position as:

$$U = r\Omega, \tag{2}$$
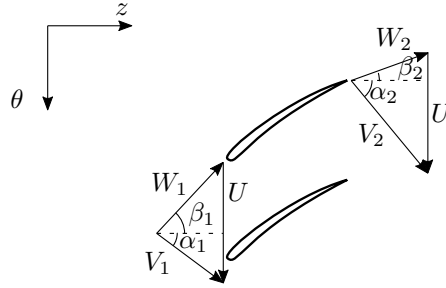
with Ω the rotation speed in rad/s.

Figure 10: Velocity and angle definitions.

The Mach numbers at the two sections are obtained from the isentropic relation between total and static pressure:

$$\frac{P_{\text{tot}}}{P_{\text{s}}} = \left(1 + \frac{\gamma - 1}{2} M^2\right)^{\frac{\gamma}{\gamma - 1}}. \tag{3}$$

The flow in the inlet duct and through the inlet guide vanes is assumed to be adiabatic. The total temperature in the upstream section is therefore equal to the ambient temperature in the lab. The knowledge of the Mach number and static temperature allows to calculate the absolute velocity in the inlet section as:

$$V_1 = M_1 c_1, \tag{4}$$

with $c = \sqrt{\gamma R T_{\text{s},1}}$ the speed of sound.

At the downstream section, temperature measurements are not available. However, the Mach number at the downstream section varies between 0.07 and 0.09 which justifies the use of the incompressible flow theory. The absolute velocity V_2 is therefore calculated as:

$$V_2 = \sqrt{\frac{2P_{\text{dyn}}}{\rho}}, \tag{5}$$

10

with ρ the density of the flow calculated using the ideal gas law with the quantities upstream of the rotor and the ideal gas constant r:

$$\rho = \frac{P_{s,1}}{RT_{s,1}} \,. \tag{6}$$

The same procedure is also valid for the upstream section, where the Mach number varies between 0.07 and 0.08.

During each measurement, the absolute flow angles α_1 and α_2 were measured. This allows to directly calculate the axial and tangential components of the absolute velocity:

$$V_z = V \cos \alpha \,, \tag{7}$$
$$V_\theta = V \sin \alpha \,. \tag{8}$$

The components of the relative velocity can then be computed as:

$$W_z = V_z \,, \tag{9}$$
$$W_\theta = V_\theta - U \,. \tag{10}$$

And finally the relative velocity and flow angle are obtained as:

$$W = \sqrt{W_z^2 + W_\theta^2} \,, \tag{11}$$
$$\beta = \arccos \frac{W_z}{W} \,. \tag{12}$$

Specific work

The specific work can be calculated from the velocities using Euler's formula:

$$\Delta h_{tot} = U(V_{\theta,2} - V_{\theta,1}) \,. \tag{13}$$

Losses

The losses can be quantified by the pressure loss coefficient:

$$\omega = \frac{P_{tot,1}^{R} - P_{tot,2}^{R}}{P_{tot,1}^{R} - P_{s,1}} \,, \tag{14}$$

where P_{tot}^{R} is the relative total pressure and is calculated as:

$$P_{tot}^{R} = P_s + \frac{\rho W^2}{2} \,. \tag{15}$$

3.3 Uncertainty

Pressure

The uncertainty on the measured pressures is caused by the resolution of the digital voltage measurement and the uncertainty of the calibration for a 95 % confidence interval:

$$\delta P = \sqrt{\left(\frac{\partial P}{\partial v} \delta v\right)^2 + (1.96\sigma_P)^2} \,, \tag{16}$$

with $\frac{\partial P}{\partial V}$ the slope of the calibration curve, δv the resolution of the voltage measurement, which is equal to $0.5\,\mu\text{V}$ in this measurement setup, and σ_P the calibration standard deviation of the pressure. The calibration standard deviation of the pressure is calculated as:

$$\sigma_P = \sqrt{\frac{\sum_{i=1}^{N} \left(\Delta P_i - \overline{\Delta P}\right)^2}{N-1}}, \tag{17}$$

in which N is the number of measurements and ΔP_i the difference between the pressure measured by the calibration instrument and the pressure predicted by evaluating the pressure calibration curve at the measured voltage.

Velocity

Because the velocity is calculated using Equation 5, its uncertainty is caused by the uncertainty on the dynamic pressure and density:

$$\delta V = \sqrt{\left(\frac{\partial V}{\partial P_{\text{dyn}}}\delta P_{\text{dyn}}\right)^2 + \left(\frac{\partial V}{\partial \rho}\delta\rho\right)^2}, \tag{18}$$

with $\delta\rho$ the uncertainty on the density and

$$\frac{\partial V}{\partial P_{\text{dyn}}} = \sqrt{\frac{1}{2P_{\text{dyn}}\rho}}, \tag{19}$$

$$\frac{\partial V}{\partial \rho} = -\sqrt{\frac{P_{\text{dyn}}}{2\rho^3}}. \tag{20}$$

Because the density is calculated using the ideal gas law (Equation 6) and because the incompressible flow assumption allows to equate the temperature $T_{\text{s},1}$ to the ambient temperature, which we assumed to be $18\,°\text{C}$, the uncertainty on the density is only caused by the uncertainty on the static pressure δP_{s}:

$$\delta\rho = \frac{\partial\rho}{\partial P_{\text{s}}}\delta P_{\text{s}} = \frac{\delta P_{\text{s}}}{RT_{\text{s},1}}. \tag{21}$$

For the axial and tangential components of the absolute velocity that are calculated using Equation 7 and Equation 8 respectively, the resolution uncertainty of the angle measurement has to be taken into account. This angle uncertainty $\delta\alpha$ is equal to $0.5°$. The resulting uncertainties on the velocities are then computed as:

$$\delta V_z = \sqrt{\left(\frac{V_z}{\partial V}\delta V\right)^2 + \left(\frac{V_z}{\partial\alpha}\delta\alpha\right)^2} \tag{22}$$

$$= \sqrt{(\cos\alpha\,\delta V)^2 + (-V\sin\alpha\,\delta\alpha)^2} \tag{23}$$

and

$$\delta V_\theta = \sqrt{\left(\frac{V_\theta}{\partial V}\delta V\right)^2 + \left(\frac{V_\theta}{\partial\alpha}\delta\alpha\right)^2} \tag{24}$$

$$= \sqrt{(\sin\alpha\,\delta V)^2 + (V\cos\alpha\,\delta\alpha)^2}. \tag{25}$$

The uncertainty on the blade velocity is caused by the resolution uncertainty of the rotation speed measurement, which is equal to 0.5 rpm or $\delta\Omega = 0.052\,\mathrm{rad/s}$. The resulting uncertainty on the blade velocity is:

$$\delta U = \frac{\partial U}{\partial \Omega}\delta\Omega = r\delta\Omega\,. \tag{26}$$

Using the previously calculated uncertainties, the uncertainties on the components of the relative velocity can be obtained:

$$\delta W_z = \delta V_z\,, \tag{27}$$

$$\delta W_\theta = \sqrt{(\delta V_\theta)^2 + (\delta U)^2}\,, \tag{28}$$

so that finally the uncertainty on the relative velocity and the relative flow angle can be computed:

$$\delta W = \sqrt{\left(\frac{\partial W}{\partial W_\theta}\delta W_\theta\right)^2 + \left(\frac{\partial W}{\partial W_z}\delta W_z\right)^2} \tag{29}$$

$$= \sqrt{\left(\frac{W_\theta}{W}\delta W_\theta\right)^2 + \left(\frac{W_z}{W}\delta W_z\right)^2}\,, \tag{30}$$

$$\delta\beta = \sqrt{\left(\frac{\partial \beta}{\partial W_z}\delta W_z\right)^2 + \left(\frac{\partial \beta}{\partial W}\delta W\right)^2} \tag{31}$$

$$= \sqrt{\left(-\frac{\delta W_z}{W\sqrt{1-\frac{W_z^2}{W^2}}}\right)^2 + \left(\frac{W_z\delta W}{W^2\sqrt{1-\frac{W_z^2}{W^2}}}\right)^2}\,. \tag{32}$$

Specific work

The specific work is calculated using Euler's formula (Equation 13). With the uncertainties of the tangential velocity components and blade velocity available, the uncertainty on the specific work is:

$$\delta h_{tot} = \sqrt{\left(\frac{\partial h_{tot}}{\partial V_{\theta,1}}\delta V_{\theta,1}\right)^2 + \left(\frac{\partial \Delta h_{tot}}{\partial V_{\theta,2}}\delta V_{\theta,2}\right)^2 + \left(\frac{\partial h_{tot}}{\partial U}\delta U\right)^2} \tag{33}$$

$$= \sqrt{(U\delta V_{\theta,1})^2 + (U\delta V_{\theta,2})^2 + [(V_{\theta,1} - V_{\theta,2})\,\delta U]^2}\,. \tag{34}$$

Losses

The losses are quantified using the loss coefficient ω defined in Equation 14. The uncertainty on the value of this loss coefficient depends on the uncertainty of the relative total pressures and upstream static pressure:

$$\delta\omega = \sqrt{\left(\frac{\partial \omega}{\partial P_{\mathrm{tot},1}^{\mathrm{R}}}\delta P_{\mathrm{tot},1}^{\mathrm{R}}\right)^2 + \left(\frac{\partial \omega}{\partial P_{\mathrm{tot},2}^{\mathrm{R}}}\delta P_{\mathrm{tot},2}^{\mathrm{R}}\right)^2 + \left(\frac{\omega}{\partial P_{\mathrm{s},1}}\delta P_{\mathrm{s},1}\right)^2}\,, \tag{35}$$

with

$$\frac{\partial \omega}{\partial P_{\text{tot},1}^{\text{R}}} = \frac{P_{\text{tot},2}^{\text{R}} - P_{\text{s},1}}{\left(P_{\text{tot},1}^{\text{R}} - P_{\text{s},1}\right)^2} \, , \tag{36}$$

$$\frac{\partial \omega}{\partial P_{\text{tot},2}} = \frac{-1}{P_{\text{tot},1}^{\text{R}} - P_{\text{s},1}} \, , \tag{37}$$

$$\frac{\partial \omega}{\partial P_{\text{s},1}} = \frac{P_{\text{tot},1}^{\text{R}} - P_{\text{tot},2}^{\text{R}}}{\left(P_{\text{tot},1}^{\text{R}} - P_{\text{s},1}\right)^2} \, , \tag{38}$$

and the uncertainty on the relative total pressure calculated as:

$$\delta P_{\text{tot}}^{\text{R}} = \sqrt{\left(\frac{\partial P_{\text{tot}}^{\text{R}}}{\partial P_{\text{s}}} \delta P_{\text{s}}\right)^2 + \left(\frac{\partial P_{\text{tot}}^{\text{R}}}{\partial \rho} \delta \rho\right)^2 + \left(\frac{\partial P_{\text{tot}}^{\text{R}}}{\partial W} \delta W\right)^2} \tag{39}$$

$$= \sqrt{(\delta P_{\text{s}})^2 + \left(\frac{W^2}{2} \delta \rho\right)^2 + (\rho W \delta W)^2} \, . \tag{40}$$

3.4   Results

Axial velocity

Figure 11a shows that in the upstream section, the axial velocity increases from hub to tip, excluding the tip regions where strong entropy gradients reduce the axial velocity according to the theory of radial equilibrium. In the downstream section, the axial velocity decreases from hub to tip.

Furthermore, we like to underline that in the computations we make the assumption of incompressible flow (because of the very low Mach numbers), meaning that the density remains constant. Despite the area being constant, we observe an offset between the axial velocities upstream and downstream. This could be due to an error in the measurement setup.

Tangential velocity

Figure 11b shows that in the upstream and downstream sections, the tangential velocity slightly decreases from hub to tip.
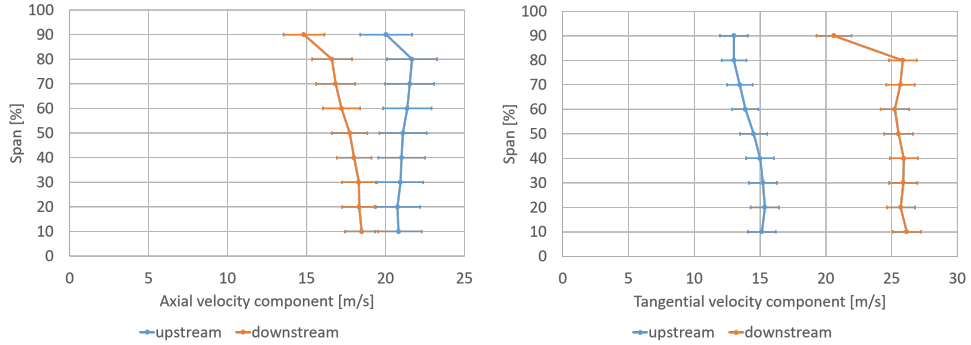
(a) Axial velocity component.   (b) Tangential velocity component.

Figure 11: Velocity profiles.

14

Angles

Figure 12a shows that the absolute flow angle decreases from hub to tip because the tangential velocity decreases, except for the tip region where the decrease of axial velocity (because of the losses) increase the flow angle. Because the compressor rotor decreases the relative flow velocity, it is correct to expect that the absolute flow angle increases from upstream to downstream. This can be observed in the graph.

Figure 12a also shows that the relative flow angle increases from hub to tip. The compressor rotor decreases the relative flow angle from upstream to downstream, which can be observed in the graph. We notice also that the uncertainty is very high, especially in the hub region. Therefore, the results are not completely reliable.

(a) Absolute flow angle.

(b) Relative flow angle.
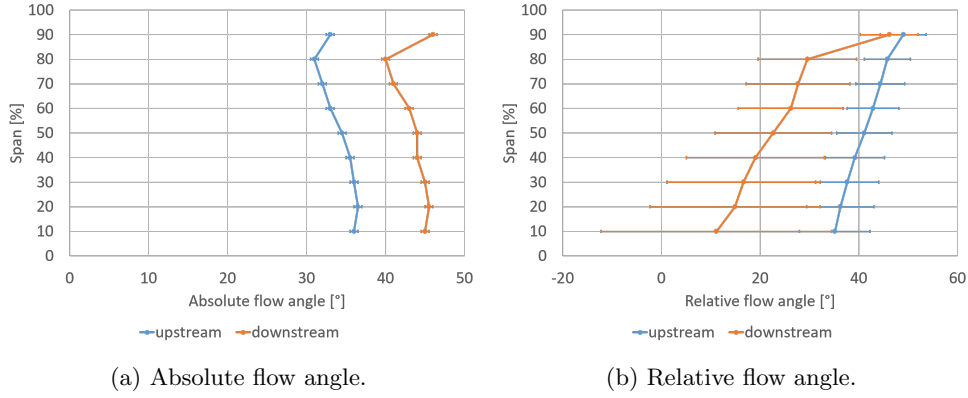
Figure 12: Angle profiles.

Total pressure

Figure 13 shows that in the upstream section, the total pressure is constant along the radius, excluding the tip regions where the boundary layer introduces losses. This is expected, we can assume that the profile losses remain constant far from the endwalls.

In the downstream section, the total pressure has increased because of the work done by the blade. We observe that the total pressure is not constant along the radius. Because of the losses at the endwalls, we expect a decrease in total pressure at the endwalls. However, because the work increases from tip to hub, we observe a bigger drop in total pressure towards the tip than towards the hub.
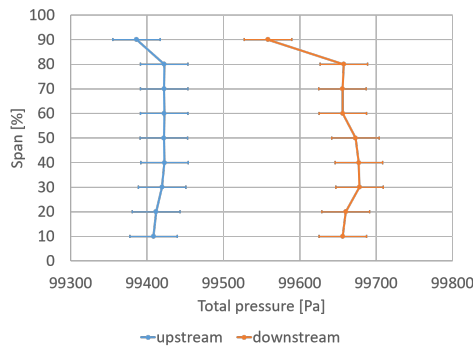

Figure 13: Total pressure

15

Specific work

Figure 14 shows that the work done by the rotor decreases from tip to hub, except near the tip where the secondary flow becomes important and reduces the work. The calculated work distribution is affected by a non-negligible uncertainty.
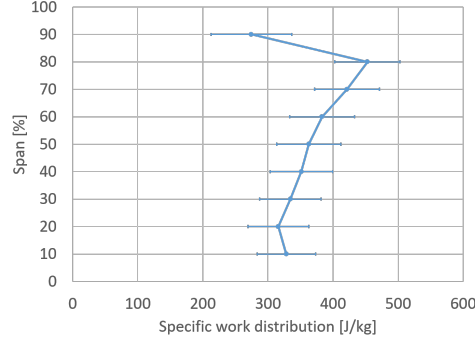

Figure 14: Specific work

Specific angular momentum

Figure 15 shows that in the upstream section, the specific angular momentum distribution can be considered constant. In the downstream section, the specific angular momentum increases from hub to tip and has a similar drop at the tip as the drop observed in the tangential velocity distribution.
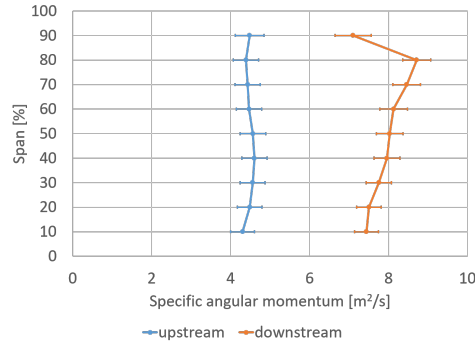
Figure 15: Specific angular momentum

Turning

Figure 16 shows that at the tip, the secondary flow induces an underturning. The uncertainty in the turning is high as a result of the high uncertainty at the relative flow angle.
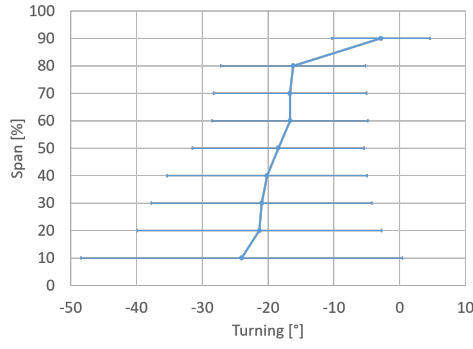
Figure 16: Turning

Losses

Figure 17 shows that the losses are smallest between mid-span and hub and increase towards the endwalls. However, because the loss coefficient is non-dimensionalized with respect to the relative velocity and because relative velocity reaches its maximum at the tip, the loss coefficient at the tip drops.
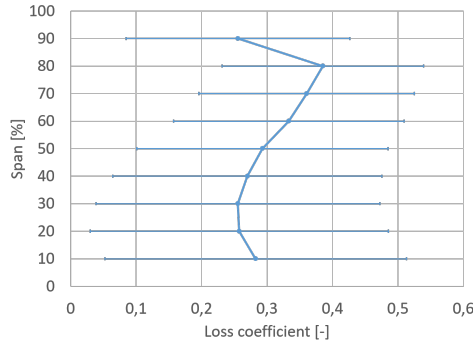

Figure 17: Loss coefficient

Conclusion

Considering these different distributions, we have good reason to believe the blades were designed using an exponential law, which has the form $A + B/r$, with A and B constants. More specifically, the following distributions show a good resemblance to the exponential law distributions:

- axial velocity upstream increases from hub to tip,
- axial velocity downstream decreases from hub to tip,
- tangential velocity upstream and downstream decreases from hub to tip,
- absolute flow angle upstream and downstream decreases from hub to tip,
- relative flow angle upstream and downstream decreases from hub to tip and
- specific angular momentum upstream and downstream increase from hub to tip.

However, there are parameters that are not in agreement with the exponential law, such as the work distribution. We would like to remind that the exponential law is a theoretical law and that in the real machine the effect of the entropy gradient can modify the ideal trend.

4 Performance measurement

4.1 Compressor performance

The compressor performance was studied by measuring total pressures upstream and downstream of the rotor for different throttle conditions. It has to be mentioned that all measurements were taken at mid-span (H=50%) for a constant rotation speed of 1000 rpm. Firstly, pressure ratios for different mass flows (throttle opening increases the mass flow) until stall are plotted. Then, the load and flow coefficients were calculated by the following relations:

$$\varphi = \frac{V_z}{U} \tag{41}$$

$$\psi = \frac{\Delta h_{tot}}{U^2} \tag{42}$$

The compressor map (Fig. 18), shows that pressure ratio is normally increasing as the mass flow decreases (throttle closes). It can also be seen that performance doesn't seem to be affected among 100%-50% of throttle opening which means that throttle doesn't affect the mass flow at this range. The maximum pressure ratio is achieved at 15% throttle opening and stall onset is observed at about 14% as the pressure ratio drops. This is because the discharge process and consequently the mass flow is interrupted.

In Fig. 19 the same behaviour is observed. As the throttle is closing, the axial velocity (V_z) is expected to decrease because the mass flow decreases. The load coefficient ψ and the pressure ratio increase from choke until stall. In the stall region itself, the pressure ratio decreases but the load coefficient keeps increasing. The work term in the load coefficient includes both the pressure increase and the energy dissipated by the losses. The pressure ratio therefore resembles the load coefficient curve, but drops in the stall region, because part of the work gets transformed to losses.

Finally, in Fig. 20 the inlet and outlet absolute Mach numbers are plotted. The inlet Mach number is decreasing as the mass flow decreases but after 50% of throttle when actually the pressure ratio starts to increase. The flow angle is imposed by the stator and stays constant. However, the axial velocity decreases because the mass flow rate decreases according to:

$$\dot{m} = \rho V_z A \,, \tag{43}$$

where the density ρ and the area A remain constant.

There is not much variation at the exit Mach number. Actually, it starts to decrease at the same point but then remains at the same levels. Outside the stall region, the two curves have similar behaviour. However, in the stall region, the formation of the formation bubble (by definition the region with zero velocity) makes the throat smaller and accelerates the flow in order to obtain the same mass flow, as is dictated by Equation 43. This results in a small increase in the Mach number downstream of the rotor.
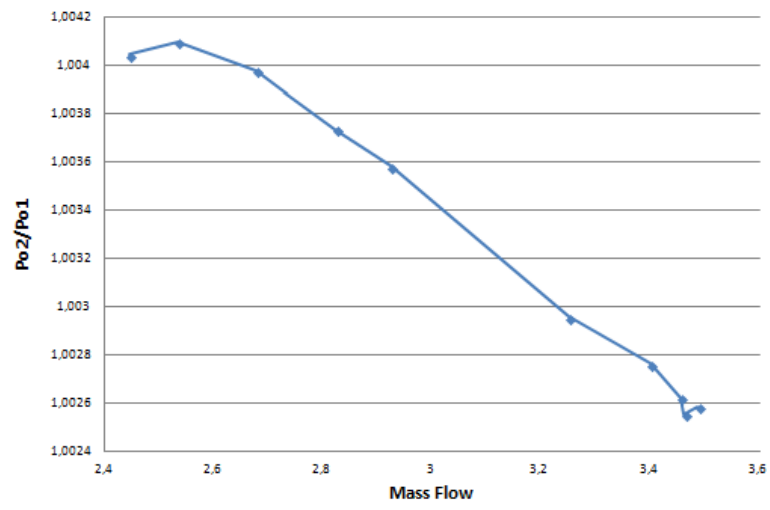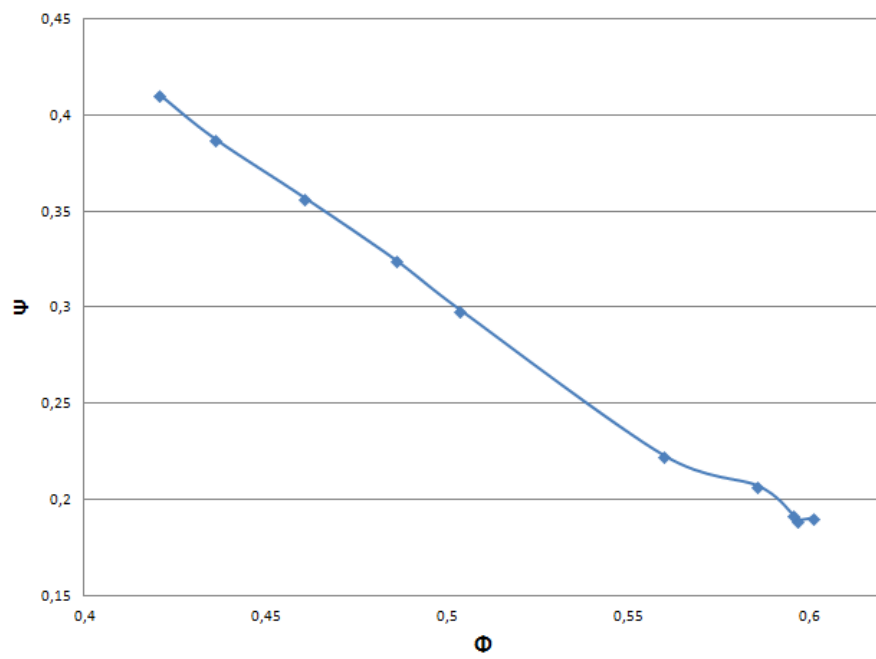
Figure 18: Compressor map

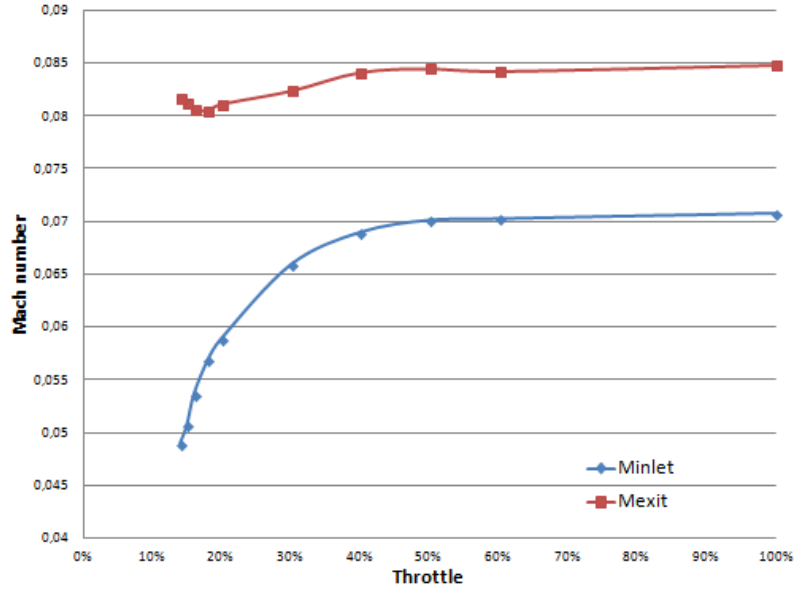Figure 19: Load coefficient vs flow coefficient

Figure 20: Inlet-Exit Mach number

4.2 Velocity fluctuation measurements

Hot wire dynamic calibration

The sampling frequency for the recording of the hot-wire signal depends on the cutoff frequency of the hot-wire system. This cutoff frequency is calculated as:

$$f_{\text{cutoff}} = \frac{1}{2.02\tau} \tag{44}$$

with τ the time the system needs to reduce the voltage increase after the peak to 37 % of the maximum voltage increase. For the hot-wire system used in this test, this voltage is equal to $0.37 \times (1.4948\,\text{V} - 1.163\,\text{V}) = 0.1228\,\text{V}$. This is attained at $127.9\,\text{µs}$ from the beginning of the response. The cutoff frequency of the hot-wire is therefore equal to $3.87\,\text{kHz}$. The sampling frequency is set at $40\,\text{kHz}$ to satisfy the Nyquist theorem.
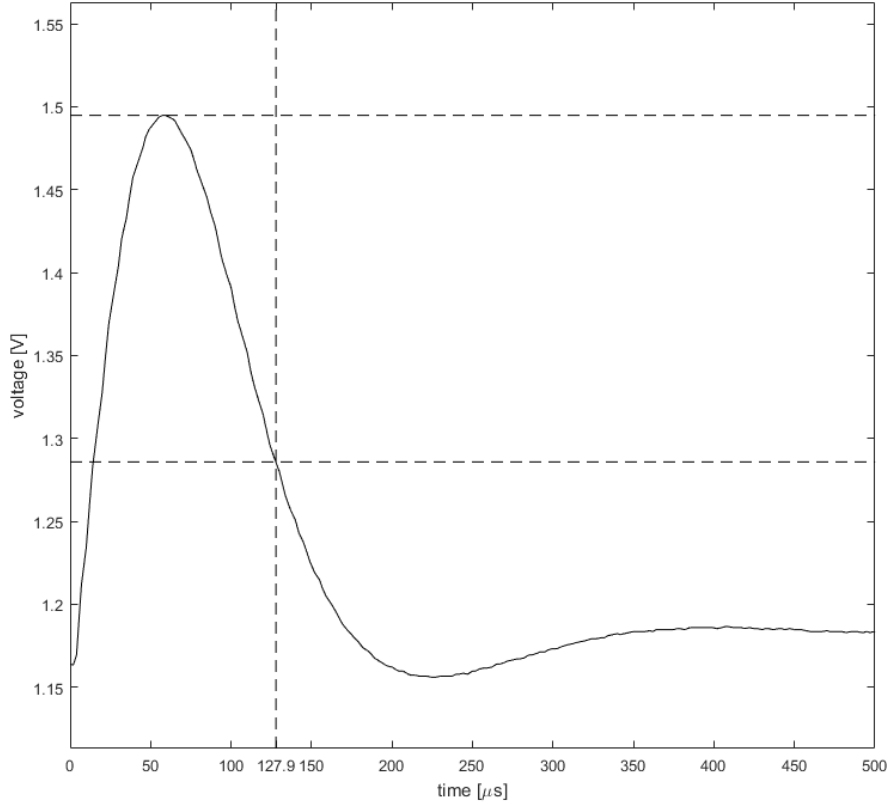
Figure 21: Hot wire response with square wave test

Time domain analysis

The performance map has been built performing several measurements at a given span position (50% in our case) and at given rotational speed decreasing the throttle's opening till. The first analysis has been performed on the time trace of the signal.

The signal has been plotted on a time interval equal to twice of the period of revolution of the machine's shaft. Since the rotational speed is equal to $\Omega = 1000\,\mathrm{rpm}$ so the period of revolution is $\frac{60}{\Omega} = 0.06s$. The first figure is the signal in function of time for a operation condition far from the stall. The signal in Fig. 22a is characterized by a strong periodicity equal to the blade passing frequency, moreover It is possible to notice a lower frequency which modulates the higher frequency signal. It is reasonable to suppose that this lower frequency is somehow related to the rotational frequency of the machine's shaft.

(a) Time trace before stall.
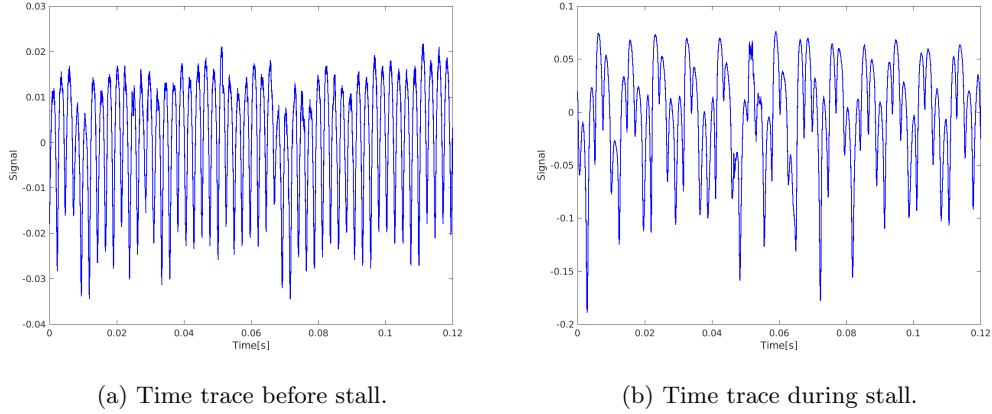(b) Time trace during stall.

Figure 22: Time trace in non stall condition (left) and after stall (right) with a time interval equal to twice the rotation period of the shaft

In Fig. 22b is reported a time trace of the hot wire's signal in correspondence of the stall conditions. Comparing Fig. 22a and Fig. 22b it is possible to notice that a new frequency appears in the signal. From a qualitative point of view it is possible to notice that the new frequency is lower than the blade passing frequency and higher than the frequency related to the rotational speed of the shaft. It is reasonable to suppose that this frequency could be related to the creation of the rotating stall cell.

Frequency domain analysis

In the previous section the time domain analysis of the signal has been presented. From the time trace it is already possible to perform a preliminary analysis of the physics involved in the stall process. In order to go deeper into details of the physics could be more convenient analyze the signal in the frequency domain instead of the time domain. The fundamental tool to switch from the time domain to the frequency domain is the Fourier Transform. In order to apply the Fourier Transform on a discrete signal has been developed the Discrete Fourier Transform, defined as:

$$X(k) = \sum_{n=0}^{N-1} x(n) e^{-i \frac{2\pi}{N} kn} \, , \tag{45}$$

where the summation is over all sampled points N ,the frequency can have only discrete value equal to $f = f_{sampling} \frac{k}{N}$ and the frequency resolution $\Delta f = \frac{f_{sampling}}{N}$. It is important to notice that the resolution in frequency is inversely proportional to the number of samples N or to the length of the acquisition interval Δt ; this feature will be exploited in the measurement near the stall where a more accurate frequency analysis is needed.

Design conditions The first spectrum we want to analyze is in correspondence of the design condition, the power spectrum is plotted in Fig. 23a. It is important to stress that we are only interested in the analysis of the location of the peaks of the spectrum and not in their amplitude, that's why the hot wire has not been calibrated for every operative condition of the compressor.

(a) Fourier transform before stall.

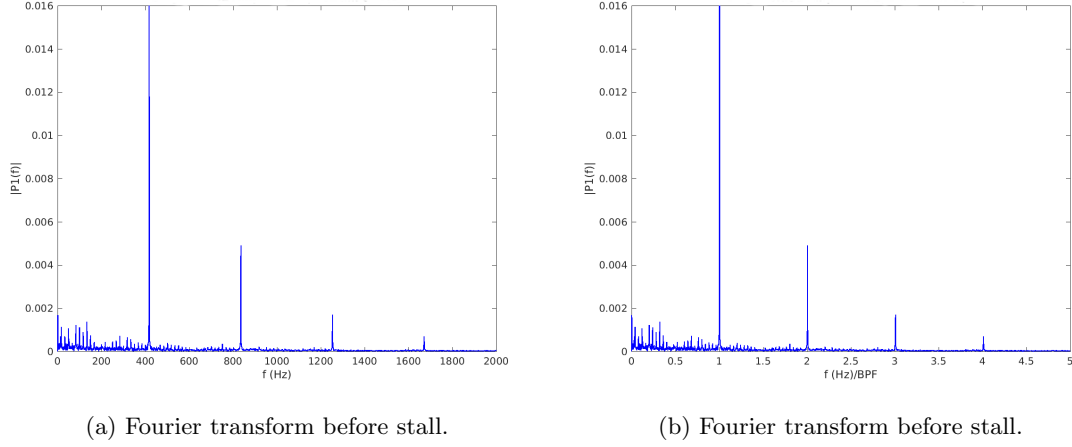(b) Fourier transform before stall.

Figure 23: Fourier Transform before stall condition: the abscissa on the left contains the absolute value of the frequencies and the abscissa on the right contains the frequencies, made non-dimensional with respect to the Blade passing frequencies, so f/BPF.
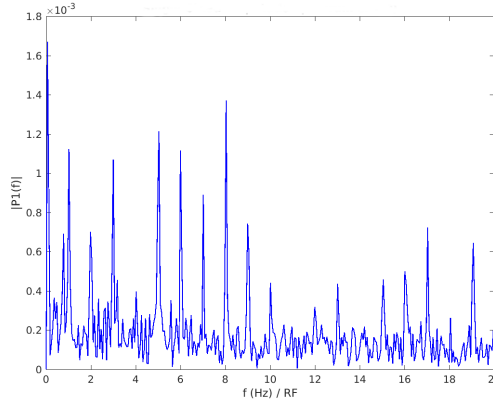

Figure 24: Zoom in the law frequencies range.

In Fig. 24 we can notice that in the flow field far from the stall two main frequency are significant:

- the first one is the blade passing frequency equal to $\text{BPF}_0 = \frac{\Omega N_b lade}{60} = 416\,\text{Hz}$. In the spectrum the blade passing frequency BPF_0 and her harmonics $\text{BPF}_n = n\text{BPF}_0$ with n integer. In order to make the plot more readable it is possible to adimensionalize the abscissa with the first harmonic of the blade passing frequency $f \longrightarrow \frac{f}{\text{BPF}_0}$ as reported in Fig. 23b where the peak are located in correspondence of integer numbers.

- the second emergent frequency is the rotational frequency, equal to $\text{RF}_0 = \frac{\Omega}{60} = 16\,\text{Hz}$, and her harmonics. Because it is much smaller than the blade passing frequency in order to visualize it better it is more convenient to zoom in the spectrum in the area of the lower frequencies. The result is reported in Fig. 23a where the abscissa is non-dimensionalized with the rotational frequency $f \longrightarrow \frac{f}{\text{RF}_0}$ in order to underline the presence of the RF and its harmonics. We can notice that there is a strong link between these two frequency in particular the ratio is equal to number of blades, this relation is verified in our case because $\frac{\text{BPF}_0}{\text{RF}_0} = 25$

23

Stall Conditions The next measurements have been performed in the stall condition; in order to reach a better frequency resolution the acquisition time has been increased from 1 second (for the measurements in the design conditions) to 2 seconds. In Fig. 25a the power spectrum is plotted: it is easy to notice the presence of an huge peak in correspondence of a frequency equal of 114 Hz (27 % of the blade passing frequency) this ratio is very close to the value of $\frac{1}{3}$ computed with the theory of nonlinear oscillations [1] so we can suppose that this peak is due to the growth of a rotating stall bubble spinning at 6840 rpm. In the same plot it is also easy to notice the presence of a little peak around 16 Hz due to the rotation of the shaft (as discuss in the previous section) and the peaks due to the blade passing frequency and its harmonics.

A quite interesting feature of the spectrum in stall conditions is that other peaks appear in the frequency domain, for example at $f = 531$ Hz and $f = 948$ Hz. These peak are correlated with the presence of the rotating stall (they were not there for the design measurement), however, their value is not a multiple of the fundamental frequency of the rotating stall so they are not its harmonics. To explain these phenomena we follow the idea proposed by Levy et al. [1].

We have already noticed that there are two main frequencies in our system: the blade passing frequency BPF $= \omega_1$ and the stall frequency SF $= \omega_2$ with $\omega_1 > \omega_2$. The basic idea is to consider the system as a non-linear system with the following two frequency signal as an input:

$$x(t) = a\sin(\omega_1 t) + b\sin(\omega_2 t)\,. \tag{46}$$

Then we approximate the non-linear transfer function of the system as:

$$f(x) = \sum_{n=0}^{N} a_n x^n\,. \tag{47}$$

Due to the non-linearity of the system, terms will appear in the output in the form of:

$$\omega_1, 2\omega_1, 3\omega_1.....\omega_2, 2\omega_2, 3\omega_2.....$$
$$\omega_1 \pm \omega_2, \omega_1 \pm 2\omega_2, \omega_1 \pm 3\omega_2.....$$
$$2\omega_1 \pm \omega_1, 2\omega_1 \pm 2\omega_2, 2\omega_1 \pm 3\omega_2.....$$

It is straightforward to extend this result to an input with more than two different frequencies.

In order to try to apply the model proposed by Levy et al. [1] to our measurements, first of all we have to understand the fundamental frequency of our system. We apply a pwelch algorithm to the signal in order to clean the signal from the noise. The main advantage of applying the pwelch on the signal is to clean the signal itself but the major drawback is the loss of resolution both from a global point of view and at low frequency (this tool does not allow us to see the lower frequency of our system such as the RF).

The result is shown in Fig. 25b and it is easy to notice that there are two fundamental frequencies: the one related to the rotating stall RSF $= 114$ Hz and the one related to the passage of the blades BPF $= 416$ Hz. To understand the structure of the spectrum we must recall the presence of the RF. In the spectrum in Fig. 26 some peaks due to the combinations of the blade passing frequency and the rotating stall frequency are clearly visible. Moreover there are also other small peaks growing around the rotating stall frequency. By measuring the value of these frequencies it is possible to relate these peak with the combination between the rotating stall frequency and the rotational frequency according to the expression: RSF $\pm n$RF, BPF $+ ($RSF $\pm n$RF$)$ and so on.
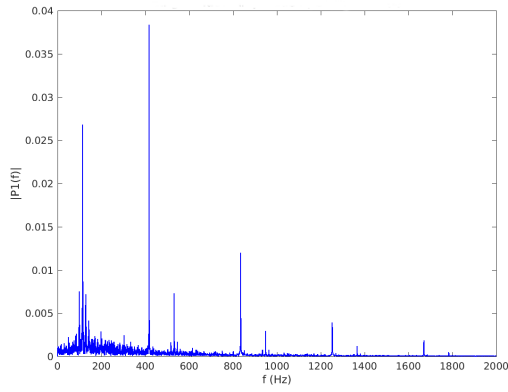
(a) Fourier transform during the stall.
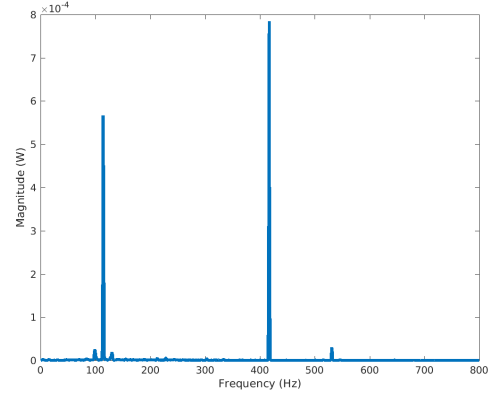
(b) PWelch of the signal.

Figure 25: On the left the Fourier Transform of the velocity signal during the stall, on the right the pwelch of the same signal.
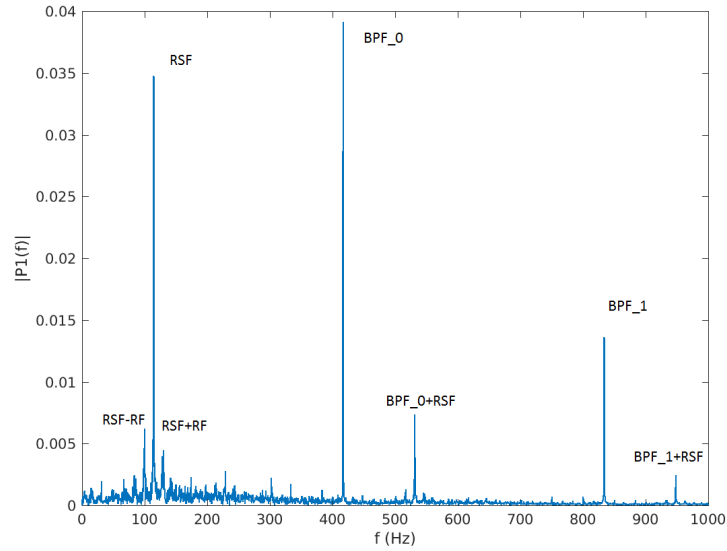

Figure 26: Zoom on the low part of the spectrum in the stall conditions.

5   Conclusion

In this measurement campaign, two sets of measurements were taken in an axial flow compressor. One set is for the flow measurement to obtain the distribution of different flow quantities along the radius. The other set is for the performance measurement of the compressor.

5.1 Flow measurement

By measuring the total and dynamic pressure and the flow angle in the upstream and downstream sections, the radial distributions of the flow quantities at 100% throttle and 1000 rpm have been reconstructed, taking the uncertainty into account. The data have been processed using the incompressible flow assumption, which is justified by very low values of the Mach number. We analyzed the kinematic quantities to deduce the vortex law used in the design of the blades and to calculate the work distribution using Euler's equation. Furthermore, we also analyzed the thermodynamic quantities to quantify the losses.

From the velocity and angle distributions, we deduced that the exponential law is the most likely vortex law for the design of the blades. This is feasible because it is a widely used design method. However, there are some discrepancies between the theoretical distributions and the measured data. These could be explained by the high uncertainty of the work distributions and high entropy gradients near the endwalls.

5.2 Performance measurement

Compressor performance

By measuring the total pressures upstream and downstream of the rotor at mid-span for different throttle conditions, the compressor map for 1000 rpm was constructed. The map showed a typical behaviour as the pressure ratio was increasing as throttle was closing and the mass flow was decreasing. Performance increased after 50% of throttle opening and stall was observed at around 14% of throttle opening. The same behaviour was also observed for the load-flow coefficient curve. Finally, the inlet absolute Mach number started to decrease for smaller throttle openings than 50% (which was the point that performance started to increase) while the exit Mach number was kept almost constant as the mass flow was decreasing.

Velocity fluctuation measurements

In this section a time and frequency domain analyses of the velocity flow field have been performed using a hot wire anemometer. The square wave test on the hot wire has been performed in order to compute the response frequency and consequently the cutoff frequency of the instrument. However there was no calibration performed on the hot wire itself so the results are relevant only for the measurement of the frequency and not the amplitude. Two different measurement have been performed: one before stall and one after stall.

- The measurement performed before stall condition clearly shows the presence of two fundamental frequencies in our system: (1) the blade passing frequency correlated to rotational speed and the number of blades and (2) the rotational frequency correlated with the rotational speed of the shaft.

- Much more interesting are the measurement in stall conditions. Here a more complex structure of the spectrum arise from the signal with a lot of high and lower peaks, the physical explanation of the presence of them is not still completely understood however some researchers develop their own theory to try to explain them. We follow the path proposed by Levy et al. [1]. The researchers model the system as a non-linear system and proved that if the input is composed of m different frequencies, the output will be the previous m frequencies, their harmonics and several combinations between the original frequencies and the harmonics. This kind of spectrum is partially reproduced in our measurements.

Bibliography

[1] Yeshayahou Levy, Asaf Medelevsky, Joseph Pismenny, Jens Friedrichs, and Detlev Wulff. *Links between Main Frequencies of Established Rotating Stall and Rotational Frequencies and/or Blade Passing Frequencies*. 2013.